

14. Baugh, C. M., Benson, A. J., Cole, S., Frenk, C. S. & Lacey, C. in *The Mass of Galaxies at Low and High Redshift* (eds Bender, R. & Renzini, A.) 91–96 (ESO Astrophysics Symposia, Berlin, Springer, 2003).

15. Rix, H. & Rieke, M. J. Tracing the stellar mass in M51. *Astrophys. J.* **418**, 123–134 (1993).

16. Bell, E. F., McIntosh, D. H., Katz, N. & Weinberg, M. D. The optical and near-infrared properties of galaxies. I. Luminosity and stellar mass functions. *Astrophys. J. Suppl.* **149**, 289–312 (2003).

17. Abraham, R. G. *et al.* The Gemini Deep Deep Survey: I. Introduction to the survey, catalogs and composite spectra. *Astron. J.* **127**, 2455–2483 (2004).

18. Savaglio, S. *et al.* The Gemini Deep Deep Survey. II. Metals in star-forming galaxies at redshift  $1.3 < z < 2$ . *Astrophys. J.* **602**, 51–65 (2004).

19. Schmidt, M. Space distribution and luminosity functions of quasi-stellar radio sources. *Astrophys. J.* **151**, 393–409 (1968).

20. Cole, S. *et al.* The 2dF galaxy redshift survey: near-infrared galaxy luminosity functions. *Mon. Not. R. Astron. Soc.* **326**, 255–273 (2001).

21. Fioc, F. & Rocca-Volmerange, B. PEGASE: a UV to NIR spectral evolution model of galaxies. Application to the calibration of bright galaxy counts. *Astron. Astrophys.* **326**, 950–962 (1997).

22. Granato, G. L. *et al.* The infrared side of galaxy formation. I. The local universe in the semianalytical framework. *Astrophys. J.* **542**, 710–730 (2000).

23. Sheth, R. K. & Tormen, G. Large-scale bias and the peak background split. *Mon. Not. R. Astron. Soc.* **308**, 119–126 (1999).

24. Somerville, R. S., Primack, J. R. & Faber, S. M. The nature of high-redshift galaxies. *Mon. Not. R. Astron. Soc.* **320**, 504–528 (2001).

25. Somerville, R. S. *et al.* The redshift distribution of near-infrared-selected galaxies in the Great Observatories Origins Deep Survey as a test of galaxy formation scenarios. *Astrophys. J.* **600**, L135–L138 (2004).

26. Stanford, S. A. *et al.* The evolution of early-type field galaxies selected from a NICMOS map of the Hubble Deep Field North. *Astron. J.* **127**, 131–155 (2004).

27. Baldry, I. K. & Glazebrook, K. Constraints on a universal stellar initial mass function from ultraviolet to near-infrared galaxy luminosity densities. *Astrophys. J.* **593**, 258–271 (2003).

28. Salpeter, E. E. The luminosity function and stellar evolution. *Astrophys. J.* **121**, 161–167 (1955).

29. Kennicutt, R. C. The rate of star formation in normal disk galaxies. *Astrophys. J.* **272**, 54–67 (1983).

30. Coleman, G. D., Wu, C.-C. & Weedman, D. W. Colors and magnitudes predicted for high redshift galaxies. *Astrophys. J. Suppl.* **43** (Suppl.), 393–416 (1980).

**Acknowledgements** This work is based on observations obtained at the Gemini Observatory, which is operated by AURA under a co-operative agreement with the NSF on behalf of the Gemini partnership: NSF (US), PPARC (UK), NRC (Canada), CONICYT (Chile), ARC (Australia), CNPq (Brazil) and CONICET (Argentina); it is also based on observations made at the Las Campanas Observatory of the Carnegie Institution of Washington. K.G. and S.S. acknowledge funding from the David and Lucille Packard Foundation; S.S. is on leave of absence from the Osservatorio Astronomica di Roma, Italy. R.A. acknowledges funding from NSERC and from the Government of Ontario through a Premier’s Research Excellence award. H.-W.C. acknowledges support by NASA through a Hubble Fellowship grant from the Space Telescope Science Institute, which is operated by the Association of Universities for Research in Astronomy, Inc., under NASA contract.

**Competing interests statement** The authors declare that they have no competing financial interests.

**Correspondence** and requests for materials should be addressed to K.G. (kgb@pha.jhu.edu).

## Old galaxies in the young Universe

A. Cimatti<sup>1</sup>, E. Daddi<sup>2</sup>, A. Renzini<sup>2</sup>, P. Cassata<sup>3</sup>, E. Vanzella<sup>3</sup>, L. Pozzetti<sup>4</sup>, S. Cristiani<sup>5</sup>, A. Fontana<sup>6</sup>, G. Rodighiero<sup>3</sup>, M. Mignoli<sup>4</sup> & G. Zamorani<sup>4</sup>

<sup>1</sup>INAF - Osservatorio Astrofisico di Arcetri, Largo E. Fermi 5, I-50125, Firenze, Italy

<sup>2</sup>European Southern Observatory, Karl-Schwarzschild-Strasse 2, D-85748, Garching, Germany

<sup>3</sup>Dipartimento di Astronomia, Università di Padova, Vicolo dell’Osservatorio, 2, I-35122 Padova, Italy

<sup>4</sup>INAF - Osservatorio Astronomico di Bologna, via Ranzani 1, I-40127, Bologna, Italy

<sup>5</sup>INAF - Osservatorio Astronomico di Trieste, via Tiepolo 11, I-34131 Trieste, Italy

<sup>6</sup>INAF - Osservatorio Astronomico di Roma, via dell’Osservatorio 2, Monteporzio, Italy

More than half of all stars in the local Universe are found in massive spheroidal galaxies<sup>1</sup>, which are characterized by old stellar populations<sup>2,3</sup> with little or no current star formation. In present models, such galaxies appear rather late in the history of the Universe as the culmination of a hierarchical merging process, in which larger galaxies are assembled through mergers

of smaller precursor galaxies. But observations have not yet established how, or even when, the massive spheroidals formed<sup>2,3</sup>, nor if their seemingly sudden appearance when the Universe was about half its present age (at redshift  $z \approx 1$ ) results from a real evolutionary effect (such as a peak of mergers) or from the observational difficulty of identifying them at earlier epochs. Here we report the spectroscopic and morphological identification of four old, fully assembled, massive ( $10^{11}$  solar masses) spheroidal galaxies at  $1.6 < z < 1.9$ , the most distant such objects currently known. The existence of such systems when the Universe was only about one-quarter of its present age shows that the build-up of massive early-type galaxies was much faster in the early Universe than has been expected from theoretical simulations<sup>4</sup>.

In the  $\Lambda$ CDM scenario<sup>5</sup>, galaxies are thought to build up their present-day mass through a continuous assembly driven by the hierarchical merging of dark matter haloes, with the most massive galaxies being the last to form. However, the formation and evolution of massive spheroidal early-type galaxies is still an open question.

Recent results indicate that early-type galaxies are found up to

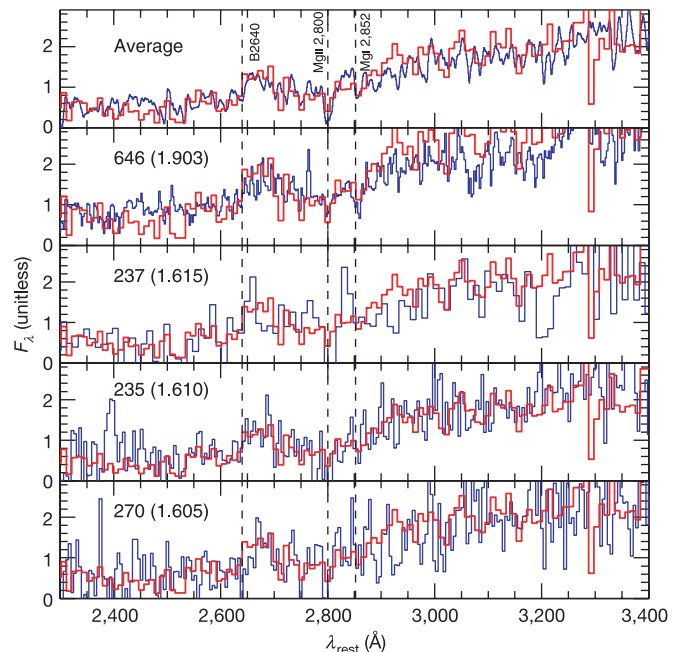


**Figure 1** The individual and average spectra of the detected galaxies. From bottom to top: the individual spectra smoothed to a 16 Å boxcar (26 Å for ID 237) and the average spectrum of the four old galaxies ( $z_{\text{average}} = 1.68$ ). The red line is the spectrum of the old galaxy LBDS 53w091 ( $z = 1.55$ ) used to search for spectra with a similar continuum shape. Weak features in individual spectra (for example, MgII 2,800 Å and the 2,640 Å continuum break, B2640) become clearly visible in the average spectrum. The object ID 235 has also a weak [OII] 3,727 Å emission (not shown here). The spectra were obtained with ESO VLT + FORS2, grisms 200I ( $R(1'') \approx 400$ ) (ID 237) and 300I ( $R(1'') \approx 600$ ) (IDs 235, 270, 646),  $1.0''$  wide slit and  $\leq 1''$  seeing conditions. The integrations times were 3 hours for ID 237, 7.8 hours for IDs 235 and 270, and 15.8 hours for ID 646. For ID 646, the ESO/GOODS public spectrum was co-added to our K20 spectrum (see Supplementary Table 1). ‘Dithering’ of the targets along the slits was applied to remove efficiently the CCD fringing pattern and the strong OH sky lines in the red. The data reduction was done with the IRAF software package<sup>16</sup>. The spectrophotometric calibration of all spectra was achieved and verified by observing several standard stars. The average spectrum, corresponding to 34.4 hours integration time, was obtained by co-adding the individual spectra convolved to the same resolution, scaled to the same arbitrary flux (that is, with each spectrum having the same weight in the co-addition), and assigning wavelength-dependent weights which take into account the noise in the individual spectra due to the OH emission sky lines.

$z \approx 1$  with a number density comparable to that of local luminous E/S0 galaxies<sup>6,7</sup>, suggesting a slow evolution of their stellar mass density from  $z \approx 1$  to the present epoch. The critical question is whether these galaxies do exist in substantial number<sup>8,9</sup> at earlier epochs, or if they were assembled later<sup>10,11</sup> as favoured by most renditions of the hierarchical galaxy formation scenario<sup>4</sup>. The problem is complicated also by the difficulty of identifying such galaxies owing to their faintness and, for  $z > 1.3$ , the lack of strong spectral features in optical spectra, placing them among the most difficult targets even for the largest optical telescopes. For example, whereas star-forming galaxies are now routinely found up to  $z \approx 6.6$  (ref. 12), the most distant spectroscopically confirmed old spheroid is still a radio-selected object at  $z = 1.552$  discovered a decade ago<sup>13,14</sup>.

One way of addressing the critical question of massive galaxy formation is to search for the farthest and oldest galaxies with masses comparable to the most massive galaxies in the present-day Universe ( $10^{11} - 10^{12} M_{\odot}$  where  $M_{\odot}$  is the solar mass), and to use them as the ‘fossil’ tracers of the most remote events of galaxy formation. As the rest-frame optical–near-infrared luminosity traces the galaxy mass<sup>15</sup>,

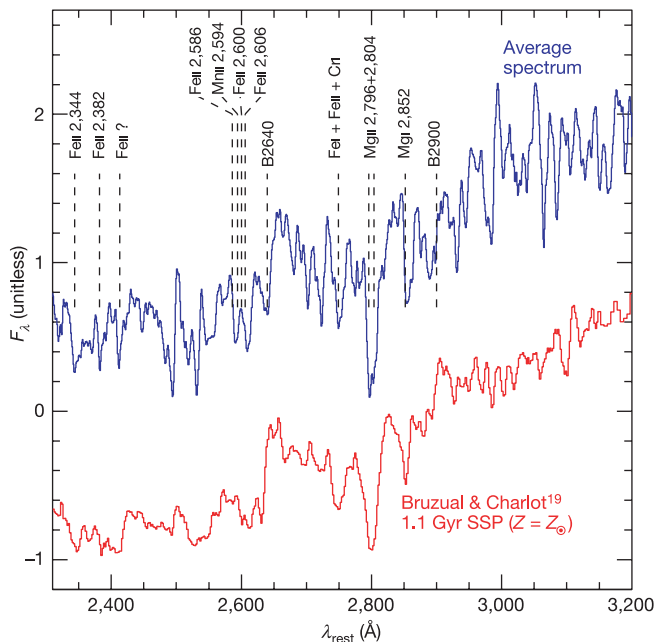


**Figure 2** The detailed average spectrum of the detected galaxies. A zoom on the average spectrum (blue) compared with the synthetic spectrum<sup>19</sup> of a 1.1-Gyr-old simple stellar population (SSP) with solar metallicity ( $Z = Z_{\odot}$ ) and Salpeter IMF (red). The observed average spectrum was compared to a library of synthetic SSP template spectra<sup>19,20</sup> with a range of ages of 0.1–3.0 Gyr with a step of 0.1 Gyr, and with assumed metallicities  $Z = 0.4 \times, 1.0 \times$  and  $2.5 \times Z_{\odot}$ . The best fit age for each set of synthetic templates was derived through a  $\chi^2$  minimization over the rest-frame wavelength range 2,300–3,400 Å. The r.m.s. as a function of wavelength used in the  $\chi^2$  procedure was estimated from the average spectrum computing a running mean r.m.s. with a step of 1 Å and a box size of 20 Å, corresponding to about three times the resolution of the observed average spectrum. The median signal-to-noise ratio is  $\sim 20$  per resolution element in the 2,300–3,400 Å range. The wavelength ranges including the strongest real features (that is, absorptions and continuum breaks) were not used in the estimate of the r.m.s. The resulting reduced  $\chi^2$  is of the order of unity for the best fit models. In the case of solar metallicity, the ranges of ages acceptable at 95% confidence level are  $1.0^{+0.5}_{-0.1}$  Gyr and  $1.4^{+0.5}_{-0.4}$  Gyr for SSP models of refs 19 and 20 respectively (see also Fig. 3, top panel). Ages  $\sim 50\%$  younger or older are also acceptable for  $Z = 2.5Z_{\odot}$  or  $Z = 0.4Z_{\odot}$  respectively. The 2,640 Å and 2,900 Å continuum break<sup>13</sup> amplitudes measured on the average spectrum are  $B2640 = 1.8 \pm 0.1$  and  $B2900 = 1.2 \pm 0.1$ . These values are consistent with the ones expected in SSP models<sup>19,20</sup> for ages around 1–1.5 Gyr and solar metallicity. For instance, the SSP model spectrum shown here has  $B2640 = 1.84$  and  $B2900 = 1.27$ .

the  $K_s$  band ( $\lambda \approx 2.2 \mu\text{m}$  in the observer frame) allows a fair selection of galaxies according to their mass up to  $z \approx 2$ .

Following this approach, we recently conducted the K20 survey<sup>16</sup> with the Very Large Telescope (VLT) of the European Southern Observatory (ESO). Deep optical spectroscopy was obtained for a sample of 546 objects with  $K_s < 20$  mag (Vega photometric scale) and extracted from an area of 52 arcmin<sup>2</sup>, including 32 arcmin<sup>2</sup> within the GOODS–South field<sup>17</sup> (hereafter the GOODS/K20 field). The spectroscopic redshift ( $z_{\text{spec}}$ ) completeness of the K20 survey is 92%, and the available multi-band photometry ( $BVRIZJHK_s$ ) allowed us to derive the spectral energy distribution (SED) and photometric redshift ( $z_{\text{phot}}$ ) of each galaxy. The K20 survey spectroscopy was complemented with the ESO/GOODS public spectroscopy (Supplementary Table 1).

The available spectra within the GOODS/K20 field were then used to search for old, massive galaxies at  $z > 1.5$ . We spectroscopically identified four galaxies with  $18 \lesssim K_s \lesssim 19$  and  $1.6 \lesssim z_{\text{spec}} \lesssim 1.9$  which have rest-frame mid-ultraviolet (UV) spectra with shapes and continuum breaks compatible with being dominated by old stars and  $R - K_s \gtrsim 6$  (the colour expected at  $z > 1.5$  for old passively evolving galaxies due to the combination of old stellar populations and k-correction effects<sup>9</sup>). Supplementary Table 1 lists the main galaxy information. The spectrum of each individual object allows a fairly precise determination of the redshift on the basis of absorption features and of the overall spectral shape (Fig. 1).

The co-added average spectrum of the four galaxies (Figs 2 and 3) shows a near-UV continuum shape, breaks and absorption lines that are intermediate between those of a F2 V and a F5 V star<sup>18</sup>, and typical of about 1–2-Gyr-old synthetic stellar populations<sup>19,20</sup>. It is also very similar to the average spectrum of  $z \approx 1$  old extremely red objects<sup>7</sup> (EROs), and slightly bluer than that of the  $z \approx 0.5$  SDSS red luminous galaxies<sup>21</sup> and of the  $z = 1.55$  old galaxy LBDS 53w091<sup>13</sup>. However, it is different in shape and slope from the average spectrum of  $z \approx 1$  dusty star-forming EROs<sup>7</sup>.

The multi-band photometric SED of each galaxy was successfully

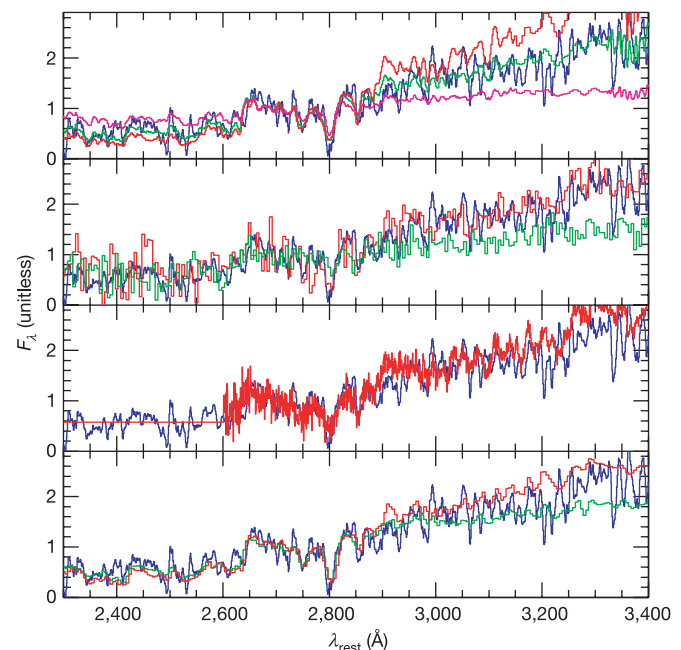


**Figure 3** The average spectrum (blue) compared to a set of template spectra. From bottom: F2 V (green) and F5 V (red) stellar spectra<sup>18</sup> with  $Z = Z_{\odot}$ , the composite spectrum (red) of 726 luminous red galaxies at  $0.47 < z < 0.55$  selected from the SDSS<sup>21</sup> (available only for  $\lambda > 2,600$  Å), the average spectra of  $z \approx 1$  old (red) and dusty star-forming (green) EROs<sup>7</sup>, SSP synthetic spectra<sup>19</sup> ( $Z = Z_{\odot}$ , Salpeter IMF) with ages of 0.5 Gyr (magenta), 1.1 Gyr (green) and 3.0 Gyr (red).

fitted without the need for dust extinction, and using a library of simple stellar population (SSP) models<sup>19</sup> with a wide range of ages, metallicity  $Z = Z_{\odot}$  and Salpeter initial mass function (IMF). This procedure yielded best-fitting ages of 1.0–1.7 Gyr, the mass-to-light ratios and hence the stellar mass of each galaxy, which results in the range of  $(1-3) \times 10^{11} h_{70}^{-2} M_{\odot}$ .  $H_0 = 70 \text{ km s}^{-1} \text{ Mpc}^{-1}$  (with  $h_{70} \equiv H_0/70$ ),  $\Omega_m = 0.3$  and  $\Omega_{\Lambda} = 0.7$  are adopted.

In addition to spectroscopy, the nature of these galaxies was investigated with the fundamental complement of Hubble Space Telescope + ACS (Advanced Camera for Surveys) imaging from the GOODS public Treasury Program<sup>17</sup>. The analysis of the ACS high-resolution images reveals that the surface brightness distribution of these galaxies is typical of elliptical/early-type galaxies (Fig. 4).

Besides pushing to  $z \approx 1.9$  the identification of the highest-redshift elliptical galaxy, these objects are very relevant to the understanding of the evolution of galaxies in general for three main reasons: their old age, their high mass, and their substantial number density.

Indeed, an average age of about 1–2 Gyr ( $Z = Z_{\odot}$ ) at  $\langle z \rangle \approx 1.7$  implies that the onset of the star formation occurred not later than at  $z \approx 2.5-3.4$  ( $z \approx 2-2.5$  for  $Z = 2.5Z_{\odot}$ ). These are strict lower limits because they follow from assuming instantaneous bursts, whereas a more realistic, prolonged star-formation activity would push the bulk of their star formation to an earlier cosmic epoch. As an illustrative example, the photometric SED of ID 646 ( $z = 1.903$ )

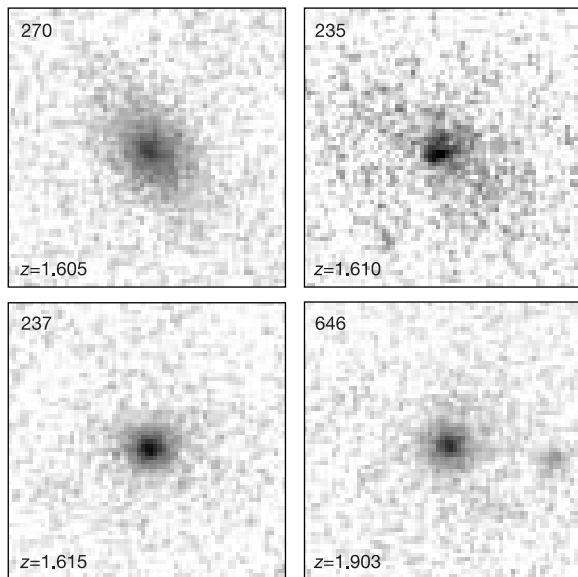


**Figure 4** The morphological properties of the detected galaxies. Images of the four galaxies taken with the Hubble Space Telescope + ACS through the F850LP filter (from GOODS data<sup>17</sup>), which samples the rest-frame  $\sim 3,000-3,500 \text{ \AA}$  for  $1.6 < z < 2$ . The images are in logarithmic grey-scale and their size is  $2'' \times 2''$ , corresponding to  $\sim 17 \times 17 \text{ kpc}$  for the average redshift  $z = 1.7$  and the adopted cosmology. At a visual inspection, the galaxies show rather compact morphologies with most of the flux coming from the central regions. A fit of their surface brightness profiles was performed with a ‘Sersic law’ ( $\propto r^{1/n}$ ) convolved with the average point spread function extracted from the stars in the ACS field and using the GASPHOT<sup>29</sup> and GALFIT<sup>30</sup> software packages. Objects ID 237 and ID 646 have profiles with acceptable values of  $n$  in the range of  $4 < n < 6$ , that is, typical of elliptical galaxies, object ID 270 is better reproduced by a flatter profile ( $1 < n < 2$ ), whereas a more ambiguous result is found for the object showing some evidence of irregularities in the morphology (ID 235,  $1 < n < 3$ ). These latter objects may be bulge-dominated spirals but no bulge/disk decomposition was attempted. Ground-based near-infrared images taken under  $0.5''$  seeing conditions with the ESO VLT + ISAAC through the  $K_s$  filter (rest-frame  $\sim 6,000-8,000 \text{ \AA}$ ) show very compact morphologies, but no surface brightness fitting was done.

can be reproduced (without dust) with either a  $\sim 1$ -Gyr-old instantaneous burst occurring at  $z \approx 2.7$ , or with a  $\sim 2$ -Gyr-old stellar population with a star-formation rate declining with  $\exp(-t/\tau)$  ( $\tau = 0.3 \text{ Gyr}$ ). In the latter case, the star-formation onset would be pushed to  $z \approx 4$  and half of the stars would be formed by  $z \approx 3.6$ . In addition, with stellar masses  $M_{\star} > 10^{11} h_{70}^{-2} M_{\odot}$ , these systems would rank among the most massive galaxies in the present-day Universe, suggesting that they were already fully assembled at this early epoch.

Finally, their number density is very high. Within the co-moving volume relative to  $32 \text{ arcmin}^2$  and  $1.5 < z < 1.9$  ( $40,000 h_{70}^{-3} \text{ Mpc}^3$ ), the co-moving density of such galaxies is about  $10^{-4} h_{70}^2 \text{ Mpc}^{-3}$ , corresponding to a stellar mass density of about  $2 \times 10^7 h_{70} M_{\odot} \text{ Mpc}^{-3}$ , that is, about 10% of the local ( $z = 0$ ) value<sup>22</sup> for masses greater than  $10^{11} M_{\odot}$ . This mass density is comparable to that of star-forming  $M_{\star} > 10^{11} M_{\odot}$  galaxies at  $z \approx 2$  (ref. 23), suggesting that while the most massive galaxies in the local Universe are now old objects with no or weak star formation, by  $z \approx 2$  passive and active star-forming massive galaxies coexist in nearly equal number.

Although more successful than previous models, the most recent realizations of semi-analytic hierarchical merging simulations still severely underpredict the density of such old galaxies: just one old galaxy with  $K_s < 20$ ,  $R - K_s > 6$ , and  $z > 1.5$  is present in the mock catalogue<sup>4</sup> for the whole five times wider GOODS/CDFS area.

As expected for early-type galaxies<sup>9,24</sup>, the three galaxies at  $z \approx 1.61$  may trace the underlying large-scale structure. In this case, our estimated number density may be somewhat biased toward a high value. On the other hand, the number of such galaxies in our sample is likely to be a lower limit owing to the spectroscopic redshift incompleteness. There are indeed up to three more candidate old galaxies in the GOODS/K20 sample with  $18.5 \lesssim K_s \lesssim 19.5$ ,  $1.5 \lesssim z_{\text{phot}} \lesssim 2.0$ ,  $5.6 \lesssim R - K_s \lesssim 6.8$  and compact HST morphology. Thus, in the GOODS/K20 sample the fraction of old galaxies among the whole  $z > 1.5$  galaxy population is  $15 \pm 8\%$  (spectroscopic redshifts only), or up to  $25 \pm 11\%$  if also all the 3 additional candidates are counted.

It is generally thought that the so-called ‘redshift desert’ around  $1.4 < z < 2.5$ ) represents the cosmic epoch when most star-formation activity and galaxy mass assembly took place<sup>25</sup>. Our results show that, in addition to actively star-forming galaxies<sup>26</sup>, a substantial number of ‘fossil’ systems also already populate this redshift range, and hence remain undetected in surveys biased towards star-forming systems. The luminous star-forming galaxies found at  $z > 2$  in sub-millimetre<sup>27</sup> and near-infrared<sup>23,28</sup> surveys may represent the progenitors of these old and massive systems.  $\square$

Received 13 February; accepted 17 May 2004; doi:10.1038/nature02668.

1. Fukugita, M., Hogan, C. J. & Peebles, P. J. E. The cosmic baryon budget. *Astrophys. J.* **503**, 518–530 (1998).
2. Renzini, A. in *The Formation of Galactic Bulges* (eds Carollo, C. M., Ferguson, H. C. & Wyse, R. F. G.) 9–26 (Cambridge Univ. Press, Cambridge, UK, 1999).
3. Peebles, P. J. E. in *A New Era in Cosmology* (eds Metcalfe, N. & Shanks, T.) 351–361 (ASP Conf. Proc. Vol. 283, Astronomical Society of the Pacific, San Francisco, 2002).
4. Somerville, R. S. *et al.* The redshift distribution of near-infrared-selected galaxies in the Great Observatories Origins Deep Survey as a test of galaxy formation scenarios. *Astrophys. J.* **600**, L135–L139 (2004).
5. Freedman, W. L. & Turner, M. S. Colloquium: Measuring and understanding the universe. *Rev. Mod. Phys.* **75**, 1433–1447 (2003).
6. Im, M. *et al.* The DEEP Groth strip survey. X. Number density and luminosity function of field E/SO galaxies at  $z < 1$ . *Astrophys. J.* **571**, 136–171 (2002).
7. Cimatti, A. *et al.* The K20 survey. I. Disentangling old and dusty star-forming galaxies in the ERO population. *Astron. Astrophys.* **381**, L68–L73 (2002).
8. Benitez, N. *et al.* Detection of evolved high-redshift galaxies in deep NICMOS/VLT images. *Astrophys. J.* **515**, L65–L69 (1999).
9. Daddi, E. *et al.* Detection of strong clustering of extremely red objects: implications for the density of  $z > 1$  ellipticals. *Astron. Astrophys.* **361**, 535–549 (2000).
10. Zepf, S. E. Formation of elliptical galaxies at moderate redshifts. *Nature* **390**, 377–380 (1997).
11. Rodighiero, G., Franceschini, A. & Fasano, G. Deep Hubble Space Telescope imaging surveys and the formation of spheroidal galaxies. *Mon. Not. R. Astron. Soc.* **324**, 491–497 (2001).
12. Taniguchi, Y. *et al.* Lyman $\alpha$  emitters beyond redshift 5: The dawn of galaxy formation. *J. Korean Astron. Soc.* **36**, 123–144 (2003).

13. Dunlop, J. S. *et al.* 3.5-Gyr-old galaxy at redshift 1.55. *Nature* **381**, 581–584 (1996).
14. Spinrad, H. *et al.* LBDS 53W091: an old, red galaxy at  $z = 1.552$ . *Astrophys. J.* **484**, 581–601 (1997).
15. Gavazzi, G., Pierini, D. & Boselli, A. The phenomenology of disk galaxies. *Astron. Astrophys.* **312**, 397–408 (1996).
16. Cimatti, A. *et al.* The K20 survey. III. Photometric and spectroscopic properties of the sample. *Astron. Astrophys.* **392**, 395–406 (2002).
17. Giavalisco, M. *et al.* The Great Observatories Origins Deep Survey: Initial results from optical and near-infrared imaging. *Astrophys. J.* **600**, L93–L98 (2004).
18. Pickles, A. J. A stellar spectral flux library: 1150–25000 Å. *Publ. Astron. Soc. Pacif.* **110**, 863–878 (1998).
19. Bruzual, G. & Charlot, S. Stellar population synthesis at the resolution of 2003. *Mon. Not. R. Astron. Soc.* **344**, 1000–1028 (2003).
20. Jimenez, R. *et al.* Synthetic stellar populations: single stellar populations, stellar interior models and primordial proto-galaxies. *Mon. Not. R. Astron. Soc.* **349**, 240–254 (2004).
21. Eisenstein, D. J. *et al.* Average spectra of massive galaxies in the Sloan Digital Sky Survey. *Astrophys. J.* **585**, 694–713 (2003).
22. Cole, S. *et al.* The 2dF galaxy redshift survey: near-infrared galaxy luminosity functions. *Mon. Not. R. Astron. Soc.* **326**, 255–273 (2001).
23. Daddi, E. *et al.* Near-infrared bright galaxies at  $z \sim 2$ . Entering the spheroid formation epoch? *Astrophys. J.* **600**, L127–L131 (2004).
24. Davis, M. & Geller, M. J. Galaxy correlations as a function of morphological type. *Astrophys. J.* **208**, 13–19 (1976).
25. Dickinson, M., Papovich, C., Ferguson, H. C. & Budavari, T. The evolution of the global stellar mass density at  $0 < z < 3$ . *Astrophys. J.* **587**, 25–40 (2003).
26. Steidel, C. C. *et al.* A survey of star-forming galaxies in the  $z = 1.4$ – $2.5$  ‘redshift desert’: Overview. *Astrophys. J.* **604**, 534–550 (2004).
27. Genzel, R. *et al.* Spatially resolved millimeter interferometry of SMM J02399-0136: A very massive galaxy at  $z = 2.8$ . *Astrophys. J.* **584**, 633–642 (2003).
28. Franx, M. *et al.* A significant population of red, near-infrared-selected high-redshift galaxies. *Astrophys. J.* **587**, L79–L83 (2003).
29. Pignatelli, E. & Fasano, G. GASPOT: A tool for automated surface photometry of galaxies. *Astrophys. Space Sci.* **269**, 657–658 (1999).
30. Peng, C. Y., Ho, L. C., Impey, C. D. & Rix, H.-W. Detailed structural decomposition of galaxy images. *Astron. J.* **124**, 266–293 (2002).

Supplementary Information accompanies the paper on [www.nature.com/nature](http://www.nature.com/nature).

**Acknowledgements** This work is based on observations made at the European Southern Observatory, Paranal, Chile, and with the NASA/ESA Hubble Space Telescope obtained at the Space Telescope Science Institute, which is operated by the Association of Universities for Research in Astronomy (AURA). We thank R. Somerville for information on the GOODS/CDFS mock catalogue. We are grateful to the GOODS Team for obtaining and releasing the HST and FORS2 data

**Competing interests statement** The authors declare that they have no competing financial interests.

**Correspondence** and requests for materials should be addressed to A.C. ([cimatti@arcetri.astro.it](mailto:cimatti@arcetri.astro.it)).

## An unusual isotope effect in a high-transition-temperature superconductor

G.-H. Gweon<sup>1</sup>, T. Sasagawa<sup>2,3</sup>, S.Y. Zhou<sup>4</sup>, J. Graf<sup>1</sup>, H. Takagi<sup>2,3,5</sup>, D.-H. Lee<sup>1,4</sup> & A. Lanzara<sup>1,4</sup>

<sup>1</sup>Materials Sciences Division, Lawrence Berkeley National Laboratory, Berkeley, California 94720, USA

<sup>2</sup>Department of Advanced Materials Science, University of Tokyo, Kashiwa, Chiba 277-8561, Japan

<sup>3</sup>CREST, Japan Science and Technology Agency, Saitama 332-0012, Japan

<sup>4</sup>Department of Physics, University of California, Berkeley, California 94720, USA

<sup>5</sup>RIKEN (The Institute of Physical and Chemical Research), Wako 351-0198, Japan

In conventional superconductors, the electron pairing that allows superconductivity is caused by exchange of virtual phonons, which are quanta of lattice vibration. For high-transition-temperature (high- $T_c$ ) superconductors, it is far from clear that phonons are involved in the pairing at all. For example, the negligible change in  $T_c$  of optimally doped  $\text{Bi}_2\text{Sr}_2\text{CaCu}_2\text{O}_{8+\delta}$  (Bi2212; ref. 1) upon oxygen isotope substitution ( $^{16}\text{O} \rightarrow ^{18}\text{O}$ )

leads to  $T_c$  decreasing from 92 to 91 K) has often been taken to mean that phonons play an insignificant role in this material. Here we provide a detailed comparison of the electron dynamics of Bi2212 samples containing different oxygen isotopes, using angle-resolved photoemission spectroscopy. Our data show definite and strong isotope effects. Surprisingly, the effects mainly appear in broad high-energy humps, commonly referred to as ‘incoherent peaks’. As a function of temperature and electron momentum, the magnitude of the isotope effect closely correlates with the superconducting gap—that is, the pair binding energy. We suggest that these results can be explained in a dynamic spin-Peierls picture<sup>2</sup>, where the singlet pairing of electrons and the electron–lattice coupling mutually enhance each other.

We compare angle-resolved photoemission spectroscopy (ARPES) data of optimally doped Bi2212 samples at the three different stages of the isotope substitution loop  $^{16}\text{O} \rightarrow ^{18}\text{O} \rightarrow ^{16}\text{O}$  (Supplementary Methods). In this way, we study directly the impact on the electron spectral function due to a modification of phonon properties, and thus gain insights into the nature of electron–phonon interaction in this material. Here we use the term ‘phonons’ loosely to denote quanta of lattice vibrations including spatially localized ones<sup>3,4</sup>. To ensure that material properties unrelated to the isotope mass did not change during the isotope substitution process, we controlled the sample growth condition with high precision (Supplementary Methods) and checked the sample quality with various post-growth characterization tools, including ARPES itself (Supplementary Figure). All ARPES data were recorded at the Advanced Light Source as detailed elsewhere<sup>5</sup>.

Figure 1 shows low temperature (25 K) ARPES spectra and their dispersions along the nodal ( $\Gamma Y$ ) direction, where the superconducting gap is zero. In this and the rest of the figures, blue, red and green represent results for  $^{16}\text{O}$ ,  $^{18}\text{O}$  and re-substituted  $^{16}\text{O}_R$  ( $^{18}\text{O} \rightarrow ^{16}\text{O}$ ) samples, respectively. In Fig. 1a, raw ARPES spectra as a function of energy (that is, the energy distribution curves, EDCs) are shown for different momenta along the nodal direction. Each EDC shows a peak, which sharpens up as momentum ( $k$ ) approaches the normal state Fermi surface<sup>6</sup>. We loosely refer to a sharp peak as a ‘coherent peak’ (CP), and a broad hump as an ‘incoherent peak’ (IP)<sup>7</sup>. We have no intention of implying that the energy and the width of CPs satisfy the Landau quasiparticle requirement. Making a comparison between the blue and red curves in Fig. 1a, we detect definite but small isotope effect. The most notable change is the shift of the peak position in curves 4 and 5 by approximately 15 meV, which is bigger than our error bar by a factor of three. Inspecting curves 1–6 in Fig. 1a, we note that the isotope effect is maximum for binding energy in the range of 100–300 meV, and vanishes as energy decreases (cut 1) and increases (cut 6) from this region. We note that this energy range coincides with range of  $J$  to  $2J$ , where  $J$  is the super-exchange interaction of neighbouring spins.

Figure 1b shows the dispersions derived from the ARPES spectra at fixed energies as a function of momentum, known as the momentum distribution curves (MDCs). As reported earlier<sup>6,8–12</sup>, we observe a ‘kink’, that is, a change of the slope in the dispersion, at energy  $\sim 70$  meV. This feature has been used as evidence that a bosonic mode renormalizes the electron dynamics<sup>13</sup>. A comparison between the  $^{16}\text{O}$  and  $^{18}\text{O}$  dispersions in Fig. 1b clearly shows that the kink separates the low-energy regime where the spectra show CP and negligible isotope effect, from the high-energy regime where the spectra show IP and appreciable isotope effect. This observation suggests that phonons contribute appreciably to the electron self energy. To illustrate the size of our error bar, we show the dispersion of the  $^{18}\text{O} \rightarrow ^{16}\text{O}$  re-substituted sample as the green line in Fig. 1b. Clearly the experimental uncertainties caused by isotope substitution are smaller than the isotope-induced changes reported here. We note that the insensitivity to isotope substitution at low energies is consistent with the notion of ‘universal nodal quasiparticle